



**We drive the development
of solutions for safer
radiation therapy**



**DELIVERY DOSAGE
ENSURED**

**INDEPENDENT VERIFICATION
DURING TREATMENT**

**OPTIMIZED CLINICAL
WORKFLOW**

A complete solution for all your patient QA needs

The Delta4 Family of products delivers Quality Assurance from prescription to final fraction.

Not only can you expect to increase your workflow efficiency but, most importantly, you can also carry out your work with full confidence that the treatment dose delivered to your patient is safe.

The Delta4 Family covers all modern treatment technologies, including VMAT, IMRT, SRS/SBRT, 4D-RT, MRgRT, bore-based linacs, Radixact and TomoTherapy.



*Innovative and Efficient QA
Delta4family.com*

Intraoperative cone-beam CT for guidance of head and neck surgery: Assessment of dose and image quality using a C-arm prototype

M. J. Daly

Ontario Cancer Institute, Princess Margaret Hospital, Toronto, Ontario, M5G 2M9 Canada

J. H. Siewerdsen^{a)}

Ontario Cancer Institute, Princess Margaret Hospital, Toronto, Ontario, M5G 2M9 Canada

Department of Medical Biophysics, University of Toronto, Toronto, Ontario, M5G 2M9 Canada

Department of Radiation Oncology, University of Toronto, Toronto, Ontario, M5G 2M9 Canada

D. J. Moseley

Ontario Cancer Institute, Princess Margaret Hospital, Toronto, Ontario, M5G 2M9 Canada

Department of Radiation Oncology, University of Toronto, Toronto, Ontario, M5G 2M9 Canada

Radiation Medicine Program, Princess Margaret Hospital, Toronto, Ontario, M5G 2M9 Canada

D. A. Jaffray

Ontario Cancer Institute, Princess Margaret Hospital, Toronto, Ontario, M5G 2M9 Canada

Department of Medical Biophysics, University of Toronto, Toronto, Ontario, M5G 2M9 Canada

Department of Radiation Oncology, University of Toronto, Toronto, Ontario, M5G 2M9 Canada

Radiation Medicine Program, Princess Margaret Hospital, Toronto, Ontario, M5G 2M9 Canada

J. C. Irish

Department of Otolaryngology-Head and Neck Surgery, University of Toronto, Toronto, Ontario, M5G 2M9 Canada

Department of Surgical Oncology, University Health Network, Toronto, Ontario, M5G 2M9 Canada

(Received 4 May 2006; revised 19 July 2006; accepted for publication 27 July 2006; published 25 September 2006)

Cone-beam computed tomography (CBCT) with a flat-panel detector represents a promising modality for intraoperative imaging in interventional procedures, demonstrating sub-mm three-dimensional (3D) spatial resolution and soft-tissue visibility. Measurements of patient dose and in-room exposure for CBCT-guided head and neck surgery are reported, and the 3D imaging performance as a function of dose and other acquisition/reconstruction parameters is investigated. Measurements were performed on a mobile isocentric C-arm (Siemens PowerMobil) modified in collaboration with Siemens Medical Solutions (Erlangen, Germany) to provide flat-panel CBCT. Imaging dose was measured in a custom-built 16 cm cylindrical head phantom at four positions (isocenter, anterior, posterior, and lateral) as a function of kVp (80–120 kVp) and C-arm trajectory (“tube-under” and “tube-over” half-rotation orbits). At 100 kVp, for example (“tube-under” orbit), the imaging dose was 0.059 (isocenter), 0.022 (anterior), 0.10 (posterior), and 0.056 (lateral) mGy/mAs, with scans at ~50 and ~170 mAs typical for visualization of bony and soft-tissue structures, respectively. Dose to radiosensitive structures (viz., the eyes and thyroid) were considered in particular: significant dose sparing to the eyes (a factor of 5) was achieved using a “tube-under” (rather than “tube-over”) half-rotation orbit; a thyroid shield (0.5 mm Pb-equivalent) gave moderate reduction in thyroid dose due to x-ray scatter outside the primary field of view. In-room exposure was measured at positions around the operating table and up to 2 m from isocenter. A typical CBCT scan (10 mGy to isocenter) gave in-air exposure ranging from 29 mR (0.26 mSv) at 35 cm from isocenter, to <0.5 mR (<0.005 mSv) at 2 m from isocenter. Three-dimensional (3D) image quality was assessed in CBCT reconstructions of an anthropomorphic head phantom containing contrast-detail spheres (11–103 HU; 1.6–12.7 mm) and a natural human skeleton. The contrast-to-noise ratio (CNR) was evaluated across a broad range of dose (0.6–23.3 mGy). CNR increased as the square root of dose, with excellent visualization of bony and soft-tissue structures achieved at ~3 mGy (0.10 mSv) and ~10 mGy (0.35 mSv), respectively. The prototype C-arm demonstrates CBCT image quality sufficient for guidance of head and neck procedures based on soft-tissue and bony anatomy at dose levels low enough for repeat intraoperative imaging, with total dose over the course of the procedure comparable to or less than the effective dose of a typical (2 mSv) diagnostic CT of the head. © 2006 American Association of Physicists in Medicine.

[DOI: 10.1118/1.2349687]

Key words: cone-beam CT, C-arm, flat-panel detector, image-guided surgery, intraoperative imaging, head and neck surgery, radiation dose, imaging performance

I. INTRODUCTION

The complexity of anatomy in the head and neck introduces significant challenges to surgical procedures in proximity to critical structures, with the risk of intracranial and orbital complications potentially impeding surgical performance, even for experienced surgeons. Systems for image-guided surgery (IGS) can provide precise intraoperative information to assist the surgeon with anatomical localization and reduce the risk of serious complication. The majority of existing IGS systems^{1–6} provide three-dimensional (3D) navigation through the use of in-room optical- or electromagnetic-based tracking systems, but typically rely on information solely from preoperative images and are therefore prone to target registration errors since the system does not account for anatomical deformation during surgery.⁷ IGS systems that can acquire intraoperative images have the benefit of providing updated anatomical information to reflect tissue deformation and the loss of anatomical landmarks during the procedure.^{8,9} IGS systems with intraoperative imaging capabilities offer the potential to improve surgical performance in existing procedures, extend the applicability of surgery to cases that would be otherwise inoperable, and support the development of novel surgical techniques that require high geometric precision.

Cone-beam computed tomography (CBCT) incorporating a flat-panel detector (FPD) offers a novel technology for intraoperative imaging.^{10,11} Flat-panel CBCT provides three-dimensional (3D) volumetric image reconstructions from 2D projections acquired in orbit about the patient and demonstrates isotropic, sub-mm 3D spatial resolution with a field of view (20–40 cm) sufficient for volumetric imaging of large anatomical sites within an open geometry. A prototype CBCT imaging system based on a mobile isocentric C-arm (PowerMobil, Siemens Medical Solutions, Erlangen, Germany) with a FPD (PaxScan 4030CB, Varian Imaging Products, Palo Alto, CA) has been developed as an experimental platform for preclinical applications in image-guided surgery and interventional radiology. Clinical applications under investigation include CBCT guidance of brachytherapy,^{11,12} spinal,¹³ orthopaedic,^{14,15} thoracic, and abdominal surgery. In head and neck surgery,^{16,17} applications under consideration include guidance of temporal bone surgery¹⁸ as well as minimally invasive approaches to the sinuses and frontal recess¹⁹ and trans-sphenoidal approaches to brain and pituitary lesions. Preclinical phantom and cadaver studies in CBCT-guided head and neck surgery have demonstrated quantitative improvements in target ablation and normal tissue avoidance in procedures for radical skull base tumor excision and total ablation of the ethmoid air cells.^{16,17}

To achieve clinical utility in IGS, intraoperative CBCT image quality must be sufficient to provide accurate guidance for a given surgical task, while ensuring that acceptably low radiation dose is delivered to patient and staff to permit repeat intraoperative imaging. In this paper, we report measurements of dose to patient and exposure to staff for intra-

operative CBCT-guided head and neck surgery and investigate 3D imaging performance for soft-tissue and bony anatomy visualization as a function of imaging dose. Two imaging phantoms were used for dose and image quality assessment: a custom-built head and neck dosimetry phantom modified from a standard 16 cm cylindrical acrylic phantom and an anthropomorphic head phantom containing contrast-detail spheres and a human skeleton for image quality evaluation. Patient dose was measured for various CBCT and fluoroscopy techniques with the dosimetry phantom in air and with a variety of patient supports (solid water, a standard operating table head extension, and a carbon fiber image-guided radiation therapy tabletop). In-room radiation exposure during CBCT acquisition was measured in air at various positions and distances from the imaging isocenter, recognizing that clinical staff are expected to move away from the setup during CBCT scanning if possible—e.g., behind a radiation shield. The effects of CBCT imaging dose, number of projections, reconstruction filter, and voxel size on quantitative (e.g., contrast-to-noise ratio) and qualitative 3D image quality were evaluated. Patient dose for intraoperative CBCT imaging was compared to typical values reported in the literature for diagnostic CT of the head. Exposure to staff was compared to occupational exposure limits and values reported for procedures in orthopaedic surgery and interventional radiology. Specific strategies to minimize dose to patient and staff and to tailor image quality to the specific head and neck surgical task are discussed.

II. MATERIALS AND METHODS

A. Mobile isocentric C-arm for flat-panel cone-beam CT

Dose and image quality measurements were acquired on a mobile isocentric C-arm (PowerMobil, Siemens Medical Systems, Erlangen, Germany) modified to provide flat-panel CBCT, as shown in Fig. 1(a). The prototype C-arm includes a large-area FPD in place of the x-ray image intensifier, a motorized orbital drive, a method for geometric calibration, and a computer control system for image acquisition and 3D reconstruction.¹³

The FPD (PaxScan 4030CB, Varian Imaging Products, Palo Alto, CA) is composed of a 2048×1536 ($\sim 40 \times 30$ cm²) active matrix of *a*-Si:H photodiodes and thin-film transistors with a $194\text{ }\mu\text{m}$ pixel pitch, 70% fill factor, and a $600\text{ }\mu\text{m}$ thick CsI:Tl scintillator. The detector can be read at frame rates up to 15 fps at full resolution, and up to 30 fps at half-resolution (1024×768 pixels at $388\text{ }\mu\text{m}$ pitch). Four readout modes are available, with various settings of gain and effective dynamic range: fixed capacitance; dual-gain interleaved (DGI); dual-gain sampling (DGS); and dynamic-gain switching.²⁰ For all studies reported below, the FPD was read at half-resolution in DGI mode.

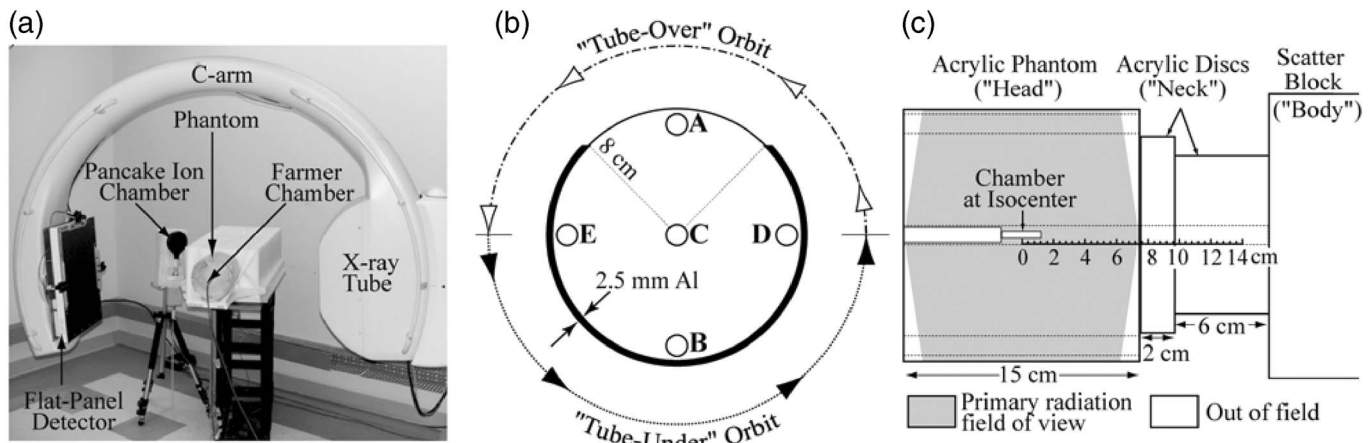


FIG. 1. (a) Experimental setup for dose and in-room exposure measurements using a prototype CBCT system consisting of a flat-panel detector (PaxScan 4030CB, Varian Imaging Products, Palo Alto, CA) on a mobile isocentric C-arm (PowerMobil, Siemens Medical Solutions, Erlangen, Germany). (b) Axial schematic diagram of a 16 cm cylindrical acrylic head phantom with 2.5 mm Al around the posterior 270° (simulating the skull at the level of the eyes). Dosimetry measurement positions (A-anterior, B-posterior, C-isocenter, D,E-lateral) and C-arm half-rotation acquisition orbits ("tube-under" and "tube-over") are illustrated. (c) Sagittal schematic of the head phantom and acrylic simulated neck. Dose to the neck outside the primary field of view was measured along the phantom longitudinal axis.

During CBCT acquisition, the system was operated in pulsed-fluoroscopic mode over a range of x-ray tube potentials (80–120 kVp) and currents (~ 0.1 –6.5 mA), with 2 mm Al and 0.1 mm Cu added filtration. At 80, 100, and 120 kVp, the first half-value layer (HVL) was 6.2, 7.4, and 8.6 mm Al, and the in-air exposure rate at isocenter was 4.0, 8.2, and 14.6 mR/mAs, measured using a R100 diode and Barracuda exposure meter (RTI Electronics, Molndal, Sweden). CBCT imaging involved collection of 2D projections (100–500) acquired with synchronized x-ray exposure and panel readout under continuous rotation of the C-arm over a source-detector orbit. The orbital range is $\sim 178^\circ$, which is less than the $180^\circ + \text{fan angle}$ ($\sim 18^\circ$) required for accurate tomographic reconstruction; therefore, image artifacts related to limited angle orbit are expected, as previously reported.¹³ Nominal CBCT acquisition involved 200 projections acquired in ~ 60 s (~ 3.3 fps). Ongoing work includes modifications to allow readout at higher frame rates to achieve faster CBCT acquisitions (e.g., 200 projections in ~ 30 s at 6.66 fps). The imaging geometry comprised a source-to-isocenter distance of 63.7 cm and a source-to-detector distance of 125.5 cm, with a magnification factor of 1.97 and a ($\sim 20 \times 20 \times 15$ cm³) volumetric field of view (FOV) at isocenter, sufficient to encompass head and neck anatomical sites. For this FOV, objects of diameter exceeding 20 cm will introduce lateral truncation artifacts. A variety of artifact reduction techniques, including extrapolation and lambda filtering methods are under investigation and are likely important in the imaging of larger body sites.¹³ For all results reported below, the x-ray beam was collimated conformal to the edges of the FPD to produce the full FOV for all dosimetry and image quality measurements.

Stationary variations in offset and gain were corrected in the projection images using 100 averaged "dark" and "flood" fields. Volume reconstructions of dimension ($256 \times 256 \times 192$) and voxel size 0.8 mm were formed from the gain-

and offset-corrected projections using a modified FDK algorithm²¹ with mechanical flex of the C-arm accommodated by a geometric calibration.²² The nominal reconstruction filter was a ramp filter in combination with a Gaussian apodization kernel, using a relative cut-off frequency $H = 0.66$ as described below. 3D reconstructions from 200 projections required ~ 150 s processing time using a research system developed in house on a Dell Precision 650 (Dual 2.0 GHz Xeon CPU; 3 GB RAM), and has been reduced to ~ 17 s using a high-speed commercially available reconstruction platform (Exxim Cobra software, 2003). Figure 2 illustrates CBCT image quality in axial, sagittal, and coronal planes along with a volume rendering of an anthropomorphic head phantom (described below).

B. Dosimetry

1. Measurement of CBCT dose

a. Dose phantom. Figure 1(b) shows an axial view of the dosimetry phantom, based on a standard 16 cm diameter cylindrical acrylic head phantom (RTI Electronics, Molndal, Sweden) with five holes (A-anterior, B-posterior, C-isocenter, D,E-lateral) for placement of the ion chamber. The anterior position A was used as an estimate of the dose to the eye lenses. The cylindrical phantom was modified to simulate the asymmetric attenuation imparted by the cranium, posterior to the orbits, based on CT images of 12 cadaver heads. Axial slices through the orbits demonstrate that the skull envelopes the posterior $\sim 270^\circ$ with an average thickness of ~ 4 mm; however, the anterior $\sim 90^\circ$ bounded by the lateral orbital walls are "unshielded" by the cranium. Accordingly, this asymmetry was simulated by incorporation of a 2.5 mm Al sheet (giving attenuation equivalent to ~ 4 mm compact bone at 50 keV) (Ref. 23) about the posterior 270° of the acrylic cylinder.

b. Source-detector orbits. C-arm half-rotation ($\sim 178^\circ$) orbits are designated below as either “tube under” (in which the x-ray tube rotates below the patient) or “tube over” (in which the x-ray tube rotates over the patient), as illustrated in Fig. 1(b). A “tube-over” orbit is accommodated by manually rotating the C-arm 180° about the source-detector axis in Fig. 1(a). CBCT imaging dose was measured at four positions within the head phantom (A–D) as a function of x-ray tube potential (80, 100, and 120 kVp) and C-arm orbit (“tube-under” and “tube-over” half rotations).

c. Dose out-of-field. It was also of interest to measure the dose delivered to regions outside the primary radiation FOV within the neck (e.g., the thyroid gland). A simulated neck was appended to the head phantom as illustrated in the sagittal view in Fig. 1(c). The neck phantom consisted of two acrylic discs (12.5 cm diameter, 2 cm long; 10 cm diameter, 6 cm long) with a measurement hole through the center, positioned between the 15 cm long head phantom and two large ($\sim 32 \times 16 \times 32 \text{ cm}^3$) polyethylene blocks simulating the body. Figure 1(c) shows that the neck phantom was outside the primary radiation FOV and contained scattered radiation only. Dose to the neck was measured by placing the ion chamber at positions (0–14 cm from isocenter) along the phantom longitudinal axis. Neck dose measurements were performed at 100 kVp and using a “tube-under” half-rotation orbit. To examine the potential benefits of shielding the neck during head imaging, measurements were repeated with a 0.5 mm Pb-equivalent thyroid collar wrapped around the acrylic neck.

d. Patient support. The “tube-under” CBCT dose measurements for (80–120 kVp) were repeated using each of the three representative patient supports (solid water slabs, a standard operating table head extension, and a carbon fiber tabletop developed for image-guided radiotherapy). The solid water slabs were 40 cm wide with a combined thickness of 2.5 cm. The operating table head extension was taken from a 55 cm wide Hercules 6500HD OR table (Skytron, Grand Rapids, MI). The carbon fiber tabletop was an Oblique Treatment Panel from an IGRT Couch Top (Aktina Medical Corporation, Congers, NY), with width 54 cm and thickness 8.5 cm. For a given CBCT technique, the “dose reduction factor” was defined as the ratio of the isocenter dose with the patient support in place, to the dose in air (i.e., with only the styrofoam support).

e. Dosimetry methods. Dose measurements were based on methods recommended by the AAPM TG-61 kV dosimetry protocol,²⁴ using a 0.6 cc Farmer ionization chamber (NE-2571) and Keithley 35040 electrometer, with air kerma calibration factor (N_k) traceable to a standard dosimetry laboratory (NRCC, Ottawa). Dose measurements (mGy) were acquired with fixed x-ray tube current ($\sim 3\text{--}4 \text{ mA}$), exposure time ($T_X=0.3 \text{ s}$), and number of projections ($N_{\text{proj}}=200$) unless otherwise mentioned. Reported CBCT dose values (mGy/mAs) are the average of three dose measurements normalized by the total mAs ($\text{mA} \times T_X \times N_{\text{proj}}$). Dose rates were highly linear ($R^2 > 0.997$) as a function of x-ray tube current and number of projections.

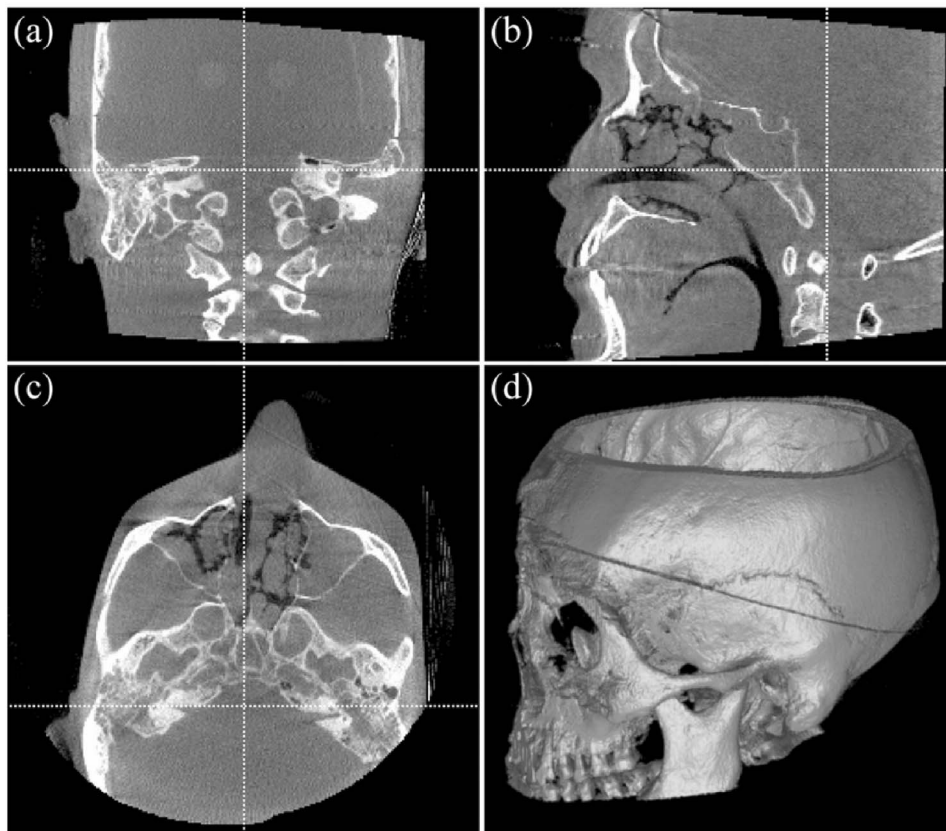


FIG. 2. (a) Coronal, (b) sagittal, (c) axial, and (d) volume renderings illustrating CBCT image quality over the ($\sim 20 \times 20 \times 15 \text{ cm}^3$) volumetric field of view (FOV). Images are of an anthropomorphic head phantom containing a natural human skeleton with soft-tissue-simulating spheres of varying diameter and contrast within the skull. The imaging technique was 100 kVp, 3.3 mA, 200 projections acquired over $\sim 178^\circ$ (200 mAs total; 11.7 mGy, as detailed below).

To compare C-arm CBCT doses with typical values reported in the literature for diagnostic head CT systems, the measured CBCT doses were converted to metrics commonly used to characterize CT systems, including the normalized weighted computed tomography dose index ($_{n\text{CTDI}_w}$), dose length product (DLP), and effective dose (E).²⁵ The $_{n\text{CTDI}_w}$ (mGy/mAs) approximates the average normalized dose to an axial slice and is given by $_{n\text{CTDI}_w} = 1/3 D_{\text{center}} + 2/3 D_{\text{periphery}}$, where D_{center} was the normalized dose at position C, and $D_{\text{periphery}}$ was the average of positions A, B, D, which are at a depth of 1 cm below the surface of head phantom. The DLP (mGy cm) is given by $\text{DLP} = _{n\text{CTDI}_w} \times \text{mAs} \times L$, where the length L for CBCT acquisition was taken to be 15 cm (i.e., the CBCT longitudinal FOV). The effective dose (mSv), a measure of the stochastic radiation risk, was estimated as $E = \text{DLP} \times E_{\text{DLP}}$, where the region-specific normalized effective dose E_{DLP} was 0.0023 mSv/(mGy cm) for the head.²⁵

2. Measurement of fluoroscopy dose

While intraoperative CBCT is expected to be the primary modality for image-guidance using the C-arm, single-shot and fluoroscopy sequences are also anticipated for guidance of head and neck surgery and other interventions (e.g., vascular procedures in the head, neck, and central nervous system), where fluoroscopy is expected to be used to a greater extent. Imaging dose during fluoroscopy acquisition was measured without C-arm rotation, at a fixed gantry angle. All other C-arm system parameters were identical to CBCT acquisition, with fluoroscopy acquired at 100 kVp and ~ 3.3 fps. Fluoroscopy dose was measured at five positions (A–E) within the head phantom for three gantry angles (LAT-lateral, PA-posterior/anterior, AP-anterior/posterior). Reported fluoroscopy doses (mGy/mAs) were measured and normalized using the same procedure described above for CBCT dose.

3. Measurement of in-room exposure

In-room exposure was measured for typical CBCT scan techniques (100 kVp, “tube-under” orbit, ~ 170 mAs, $N_{\text{proj}} = 200$, 60 s scan time) at positions immediately surrounding the dosimetry phantom and up to 2 m from the isocenter. Experiments were conducted in a radiation-shielded room of dimension ($\sim 3.9 \times 2.6$ m²). The positions around the phantom include typical locations of surgical staff around an operating table during a head and neck procedure, including three anesthesiologist positions (T1–T3, 35–40 cm superior of the isocenter), the surgeon (T4, 40 cm lateral of the isocenter), a nurse (T5, 70 cm from the isocenter, adjacent to the surgeon), and two surgical assistants (T6 and T7, 50 and 80 cm from the isocenter, opposite the surgeon). While in-air exposure measurements at these locations are important, in clinical use staff would step away from the system during CBCT acquisition whenever possible (e.g., leaving the surgical suite or standing behind modular shield walls), or would wear proper radiation shielding apparel in accordance with as-low-as-reasonably-achievable (ALARA) principles.

In-air exposure was also measured around concentric circles at radial distances 1, 1.5, and 2 m from the isocenter to demonstrate the reduction in exposure with distance. All measurement positions were outside of the imaging FOV and detected only scattered radiation.

Exposure (mR) was measured using a 180 cc pancake exposure detector (Radiation Monitor Control Model 9015, Radcal Corp., Monrovia, CA) directed toward the isocenter at a height of 1 m (approximately waist height and at the same level as the isocenter). The exposure measurements were made “in air,” and therefore quantify the entrance exposure to staff (without attenuation introduced by the body or x-ray shielding devices). Reported exposures (mR/mGy) are normalized by the CBCT dose to isocenter. To compare with typical unshielded exposures reported in the literature, in-air exposures X (mR) were converted to effective dose $E_{\text{unshielded}}$ (mSv), using $E_{\text{unshielded}} = X \times f / 100$, where an f -factor f of 0.9 was used.²⁶ Estimates of the effective dose with personnel shielding E_{shielded} (mSv), assuming a 0.5 mm Pb-equivalent apron and thyroid shield, were calculated using $E_{\text{shielded}} = 1.5 \times E_{\text{body}} + 0.04 \times E_{\text{head}}$,²⁷ where dose to the unshielded head was assumed to be $E_{\text{head}} = E_{\text{unshielded}}$, and dose to the shielded body was calculated as $E_{\text{body}} = 0.1 \times E_{\text{unshielded}}$ for an apron providing 90% reduction in dose.²⁸

C. Image quality

1. Image quality phantom

The experimental setup for image quality measurements was identical to the dosimetry setup, except the dosimetry phantom was replaced by an anthropomorphic head phantom²⁹ suspended in air. The phantom contains two layers of soft-tissue-simulating spheres of variable contrast (11–103 HU; 12.7 mm diameter) and variable diameter (1.6–12.7 mm; 84 HU contrast to uniform background), allowing for quantitative and qualitative evaluation of image quality in 3D CBCT reconstructions. The phantom also incorporates a natural human skeleton for qualitative assessment of bony detail visualization. Image quality was evaluated by quantitative analysis of contrast-to-noise ratio (CNR) and qualitative assessment of soft-tissue and bony visualization (as assessed by two physicists and one surgeon). A quantitative assessment of visibility by receiver operating characteristic (ROC) tests or the like is beyond the scope of current investigation.

2. CNR analysis

For quantitative evaluation of imaging performance, contrast, noise, and CNR were analyzed in each of the variable-contrast (fixed-diameter) spheres. To analyze CNR, two regions of interest (ROI) were identified in each axial slice—one (7×7) voxel region within the sphere, and the other formed from a set of eight (3×3) regions in the immediately adjacent background (evenly spaced on a circle with a 12 voxel radius from the sphere center). The mean ($\bar{\mu}_{\text{sphere}}$ and $\bar{\mu}_{\text{background}}$) and standard deviation (σ_{sphere} and $\sigma_{\text{background}}$) of voxel values in each ROI was computed in ten axial slices, and then normalized by the average of the means in the

sphere and background ROIs: $(\bar{\mu}_{\text{sphere}} + \bar{\mu}_{\text{background}})/2$. The normalization enables assessment of relative contrast and noise independent of any absolute scaling of voxel intensity as reported by the reconstruction software. Contrast (C) was defined as the absolute difference between the mean voxel values of the sphere and background: $C = |(\bar{\mu}_{\text{sphere}} - \bar{\mu}_{\text{background}})|$. The voxel noise (σ) was taken as the average of the standard deviation in the sphere and background ROIs: $\sigma = (\sigma_{\text{sphere}} + \sigma_{\text{background}})/2$, CNR was simply C/σ , reported as an average of the values computed across the axial slices. The resulting CNR is independent of the normalization factor used to scale the means and standard deviations. Error bars represent two standard deviations in CNR as determined over the ten axial slices.

3. Soft-tissue and bony visualization

For qualitative assessment of soft-tissue visualization, images of contrast-detail spheres on a single axial slice are displayed with equivalent grayscale window and level throughout for fair intercomparison. Three regions within the anthropomorphic phantom were selected to assess bony anatomy visualization: an axial view of the skull base (including the clivus and sphenoid sinus); a sagittal view of the paranasal sinuses (including the frontal sinus, cribriform plate, ethmoid air cells, pituitary gland, sphenoid sinus, and clivus); and an axial view of the temporal bone (including the mastoid air cells, external auditory canal, and cochlea).

4. Parameters affecting image quality

The effects of the following acquisition, reconstruction, and post-processing parameters on CBCT imaging performance were evaluated:

a. Effect of CBCT dose. 3D volume reconstructions were acquired as a function of dose by varying the x-ray tube current while fixing other CBCT acquisition parameters (100 kVp, $N_{\text{proj}}=200$, “tube-under” C-arm orbit), resulting in a range of ~ 10 –395 mAs. The CBCT dose within the anthropomorphic head phantom for a given CBCT technique was calculated from the corresponding normalized dose measurement (mGy/mAs) within the dosimetry phantom, giving a range of 0.6–23.3 mGy over the range of tube current acquisitions investigated. CNR as a function of dose was analyzed in each of the variable-contrast (12.7 mm diameter) spheres.

b. Effect of number of projections. CBCT image quality was evaluated as a function of the number of projections N_{proj} at three dose levels (~ 1.5 , ~ 3.6 , and ~ 11.7 mGy). Three CBCT acquisitions ($N_{\text{proj}}=100, 200, 500$) were acquired per dose level, using 100 kVp and “tube-under” orbit. The choice of N_{proj} also has an effect on the CBCT acquisition time while operating at 3.3 fps: “Fast” (100 projections in 30 s); “Nominal” (200 projections in 60 s); and “Slow” (500 projections in 150 s). The x-ray tube current was adjusted for each of the three CBCT techniques to produce approximately equal imaging dose ($\sim \pm 4\%$), and therefore allow intercomparison of image quality as a function of N_{proj} (but equal total dose). Soft-tissue visualization is evaluated

in images of the variable-contrast (12.7 mm diameter) spheres reconstructed with the nominal 0.8 mm voxel size. To better investigate the influence of view aliasing artifacts expected at low N_{proj} axial images of the temporal bone region near the periphery of the head were reconstructed with a higher resolution voxel size of 0.2 mm.

c. Effect of reconstruction filter. The effect of the reconstruction filter on CBCT image quality was evaluated for four choices of convolution kernel. The reconstruction filters consist of a ramp filter in combination with a normalized Gaussian apodization of the form: $T(f) = (1/2\pi) \times \exp(-\pi k f^2/H)$, characterized by the relative cut-off frequency H . To examine the inherent tradeoffs between image noise and spatial resolution with the choice of parameter H , four cut-off frequencies were evaluated: $H=0.11$ (“smooth” filter), $H=0.20$, $H=0.33$, and $H=0.66$ (“sharp” filter). CBCT reconstructions using each of the filters were generated from the projection sets acquired as a function of dose (0.6–23.3 mGy), as described in Sec. C.4.

d. Effect of voxel size. The effect of axial slice averaging on CBCT image quality was evaluated for four choices of axial slice thickness. Nominal CBCT reconstructions of dimension $(256 \times 256 \times 192)$ and voxel size 0.8 mm were generated from the projection sets (0.6–23.3 mGy) described in Sec. C.4. Slice averaging was performed as a simple post-processing procedure to reduce image noise, with a corresponding tradeoff in decreased spatial resolution and potential partial-volume artifacts. The number of averaged axial slices was varied over the range 1 (no averaging) to 4, resulting in axial slice thicknesses Δz_{slice} over the range 0.8–3.2 mm.

III. RESULTS

A. Dosimetry

1. Measurement of CBCT dose

CBCT dosimetry results are summarized in Fig. 3. CBCT dose for the “tube-under” orbit at each of the four measurement positions (A–D) within the 16 cm head phantom increased as a second-order polynomial with kVp, as shown in Fig. 3(a). Normalized dose for “tube-under” CBCT acquisition at 100 kVp was 0.059 (isocenter), 0.022 (anterior), 0.10 (posterior), and 0.056 (lateral) mGy/mAs. Computing the absolute imaging dose using, for example, a typical CBCT technique of 170 mAs ($\text{mA} \sim 2.8$; $T_x=0.3$ s; $N_{\text{proj}}=200$) results in doses of 10.0 (isocenter), 3.7 (anterior), 17 (posterior), and 9.5 (lateral) mGy. The $(\text{C}_n \text{CDTI}_w)$ for 80, 100, and 120 kVp were 0.025, 0.059, 0.11 mGy/mAs, respectively, which are approximately equal (within 3%) to the measured doses at isocenter.

Figure 3(b) shows dose for “tube-under” and “tube-over” orbits at 100 kVp. The normalized dose for “tube-over” orbit was 0.063 (isocenter), 0.12 (anterior), 0.024 (posterior), and 0.056 (lateral) mGy/mAs. Comparison of “tube-under” and “tube-over” orbits indicates that dose to the eyes (anterior

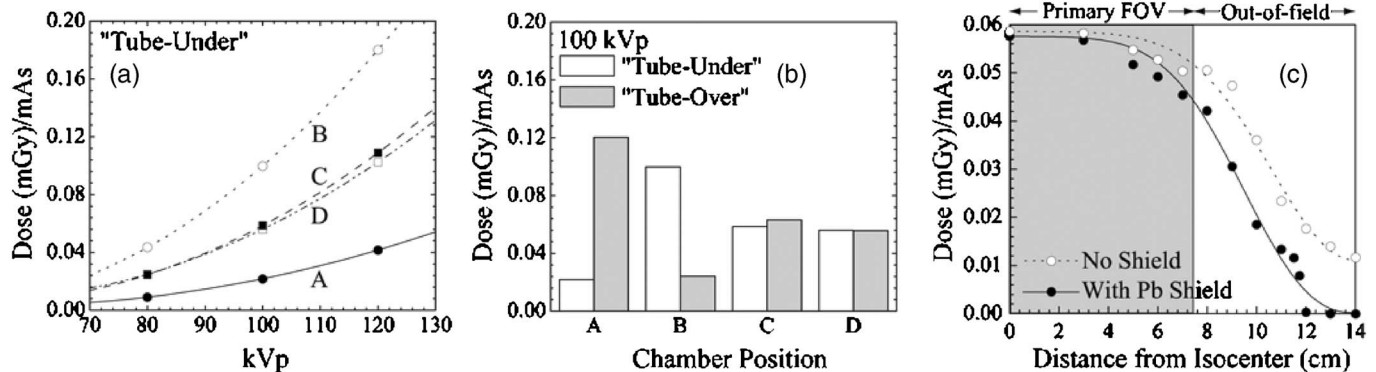


Fig. 3. (a) CBCT dose (mGy/mAs) at four positions (A–D) within the head phantom as a function of x-ray tube potential ("tube-under" orbit). (b) Comparison of dose for "tube-under" and "tube-over" orbits at the four positions (at 100 kVp). Significant dose sparing to the eyes (position A) was achieved using the "tube-under" orbit. (c) Dose as a function of distance from isocenter with and without a 0.5 mm Pb-equivalent thyroid shield wrapped around acrylic "neck" (100 kVp; "tube-under"). Significant dose is observed at up to 7 cm out-of-field, with a moderate reduction at extended distances provided by the Pb shield.

position A) was reduced by a factor of ~ 5 for "tube-under" (0.022 mGy/mAs) versus "tube-over" (0.12 mGy/mAs) orbits.

Figure 3(c) shows dose as a function of distance from the isocenter along the phantom longitudinal axis with and without a 0.5 mm Pb-equivalent thyroid shield wrapped around the acrylic neck. Significant dose ($> \sim 20\%$ of the dose at the isocenter) due to scattered radiation was observed at distances up to 7 cm outside the primary radiation field of view, with some dose reduction ($\sim 40\text{--}100\%$) at extended distances provided by the Pb shield. The results suggest that the addition of a thyroid shield provides moderate sparing of the thyroid; however, for a well-collimated beam, the dose is largely due to scattered x rays originating within the skull and traveling longitudinally down the neck.

2. Effect of patient supports on CBCT dose

The "tube-under" CBCT dose reduction factors for three representative patient supports as a function of 80–120 kVp are summarized in Fig. 4. The 2.5 cm thick solid water slabs reduced the CBCT isocenter dose to 70–74 % of the measured (head-in-air) value. The operating room (OR) table head extension and the carbon fiber table reduced the CBCT dose to 65–74 % and 80–82 % of the nominal "tube-under" values, respectively. In practice, kVp and/or x-ray tube current can be adjusted to compensate for the attenuation of the patient support to achieve a given level of patient dose and image quality. In that sense, the magnitudes of the dose reduction factors (e.g., larger values for the carbon fiber table, smaller values for the OR table extension) are not intended to indicate which table is preferred for CBCT imaging in terms of dose to patient; however, supports with less attenuation have the benefit of reducing the heat load on the x-ray tube. Investigation of the relative merits of various supports (e.g., reduced truncation artifacts, x-ray scatter, etc.) is beyond the scope of these studies.

Note that the patient support only reduces the CBCT dose for a "tube-under" orbit. For a "tube-over" orbit, attenuation by the table results in no change to CBCT dose compared to the styrofoam support. Exposure to the detector is equivalent

for both "tube-under" and "tube-over" orbits; however, for a given level of patient dose, image quality is higher for the "tube-under" orbit (ignoring differences in beam hardening and x-ray scatter), since the support attenuates prepatient x-rays, rather than transmitted fluence. Conversely, the "tube-under" orbit offers reduced patient dose at equivalent image quality.

3. Measurement of fluoroscopy dose

Fluoroscopy dosimetry results are summarized in Fig. 5, including an illustration of the x-ray source positions for the three gantry angles (LAT-lateral, PA-posterior/anterior, AP-anterior/posterior). The maximum dose for each gantry angle were found at the head positions in closest proximity to the x-ray source—viz., AP (0.16 mGy/mAs at A), LAT (0.14 mGy/mAs at E), and PA (0.14 mGy/mAs at B). The

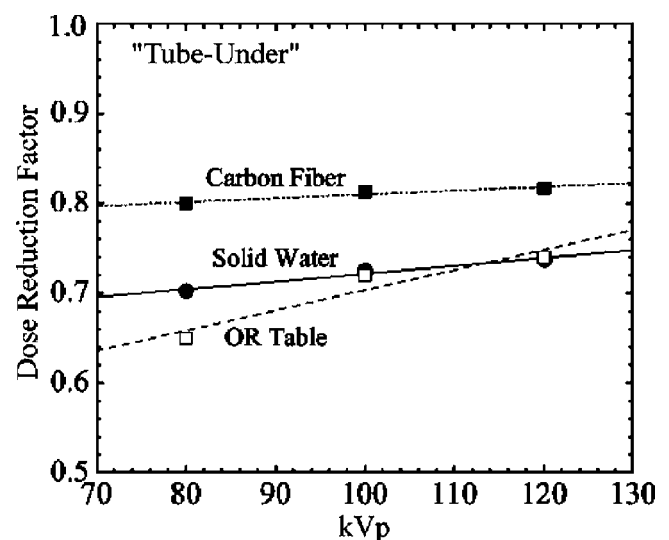


Fig. 4. Dose reduction factors (i.e., ratio of CBCT dose at isocenter with and without patient support under the head phantom) for three representative patient supports (a 2.5 cm thick solid water slab, a standard operating table head extension, and a carbon fiber table for image-guided radiation therapy) as a function of x-ray tube potential using "tube-under" orbit.

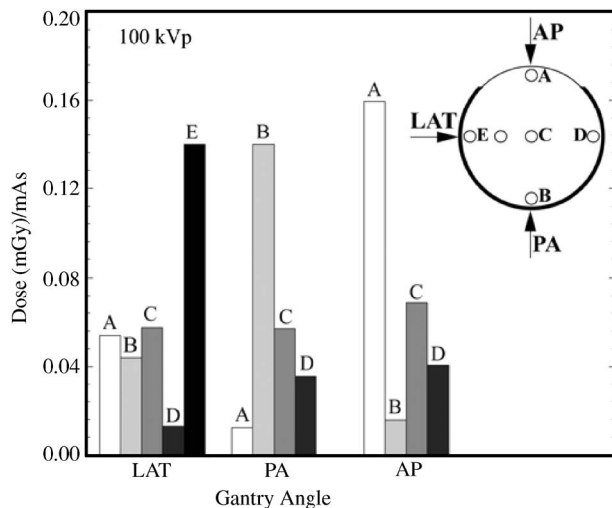


FIG. 5. Fluoroscopy dose (mGy/mAs) for three source-detector gantry angles (LAT-lateral, PA-posterior/anterior, AP-anterior/posterior) measured at five positions within the head phantom (A–E) at 100 kVp. The dose at position E for PA and AP angles is assumed equivalent to the dose at D.

asymmetry imparted by the simulated skull results in a slightly higher maximum dose for AP (0.16 mGy/mAs), compared to LAT and PA (0.14 mGy/mAs). Comparison of the dose to the anterior position A from AP (0.16 mGy/mAs) and PA (0.012 mGy/mAs) makes evident that significant dose sparing to the eyes (i.e., a factor of ~ 13) can be achieved using PA acquisition for fluoroscopy.

The fluoroscopy dose to isocenter for the two gantry angles along the CBCT “tube-under” orbit (LAT, PA: 0.057 mGy/mAs at C) are approximately equivalent to the CBCT “tube-under” dose at 100 kVp (0.059 mGy/mAs). Gantry flex during CBCT orbital motion may contribute to the observed difference ($\sim 3\%$) between fluoroscopy and CBCT dose, which would be otherwise equivalent. Therefore, the dose to isocenter from a nominal CBCT acquisition (200 projections in 60 s) is approximately equivalent to 200 frames of fluoroscopy (at equivalent technique).

4. Measurement of in-room exposure

In-room exposure measurements are illustrated in Fig. 6. The measured exposures at marked positions were interpolated over the entire room, shown by the colorscale. Total exposure for a 10 mGy scan ranged from 29 mR (0.26 mSv) at 35 cm from the isocenter (T2), to <0.5 mR (<0.005 mSv) at 2 m from isocenter. The in-room exposure declined steeply as a function of distance from isocenter (e.g., at distances 1, 1.5, and 2 m along a ray perpendicular to the C-arm orbital motion the normalized exposures were 0.29, 0.13, and 0.07 mR/mGy.) Normalized exposures immediately around the dosimetry phantom were 2.50 (T1), 2.88 (T2), 2.04 (T3), 1.55 (T4), 0.26 (T5), 0.22 (T6), and 0.91 (T7) mR/mGy. For the “tube-under” CBCT acquisition used for exposure measurements, the presence of the large polyethylene scatter blocks (simulated “body”) and optical bench supporting the phantom setup provide some degree of

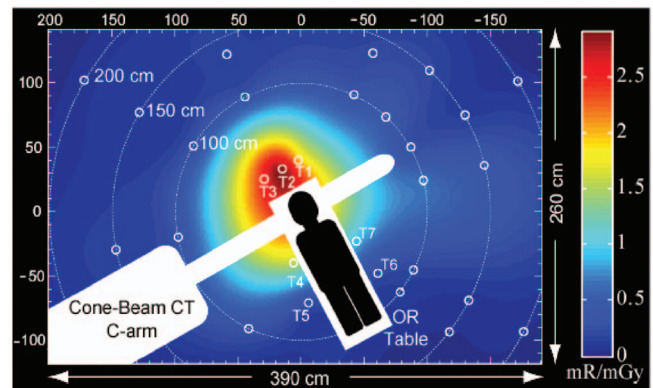


FIG. 6. Illustration of accumulated in-air radiation exposure for CBCT scanning (100 kVp; “tube-under”) measured at various positions and distances from isocenter. Measurement points are marked by white circles, interpolated over the entire room as shown by the colorscale. Values refer to in-air exposure (mR) per unit dose to isocenter (mGy). Positions around the operating table are typical locations of surgical staff during a head and neck procedure: anesthesiologist (T1, T2, T3), surgeon (T4), nurse (T5), and surgical assistants (T6, T7). During CBCT acquisition, however, it is expected that staff would leave the room, move behind shield walls, and/or wear shielded apparel consistent with ALARA principles.

radiation shielding for positions T4–T7, as compared to positions T1–T3 immediately superior to the head.

B. Image Quality

1. Effect of CBCT dose

Figures 7 and 8 illustrate the effect of CBCT dose on the visualization of low-contrast, soft-tissue-equivalent spheres and high-contrast, bony anatomy, respectively. Figure 7(a) shows CNR as a function of CBCT dose for each of the variable-contrast spheres (11–103 HU). As expected, image noise varied as the inverse square root of dose,³⁰ absolute contrast was independent of dose, and as a result, CNR increased as the square root of dose.

Axial images of the variable-contrast (fixed-diameter) and variable-diameter (fixed-contrast) spheres acquired at four dose levels ranging 0.6–23.3 mGy are shown in Fig. 7(b). At 0.6 mGy, image noise prevents detection of almost all of the spheres, except the higher contrast ($> \sim 66$ HU) spheres with diameter 12.7 mm. At 2.9 mGy, the detection of $> \sim 45$ HU spheres is feasible, while at 9.6 mGy spheres $> \sim 22$ HU are visible. The image quality at the highest dose (23.3 mGy) does not demonstrate a significant improvement as compared to the images at 9.6 mGy, indicating that an imaging dose of ~ 10 mGy is sufficient for visualization of soft-tissue structures of contrast $> \sim 22$ HU and diameter $> \sim 3.2$ mm.

The 3D segmentation of bony anatomy shown in Fig. 8(a) illustrates the uniform image quality achieved within the volumetric FOV encompassing the anthropomorphic head phantom. Figure 8(b) shows sagittal images of the paranasal sinuses and axial images of the skull base at the same dose levels as in Fig. 7 (0.6–23.3 mGy). At 0.6 mGy, visualization is severely impaired for both the sinuses and skull base. Even at this low imaging dose, however, some high-contrast

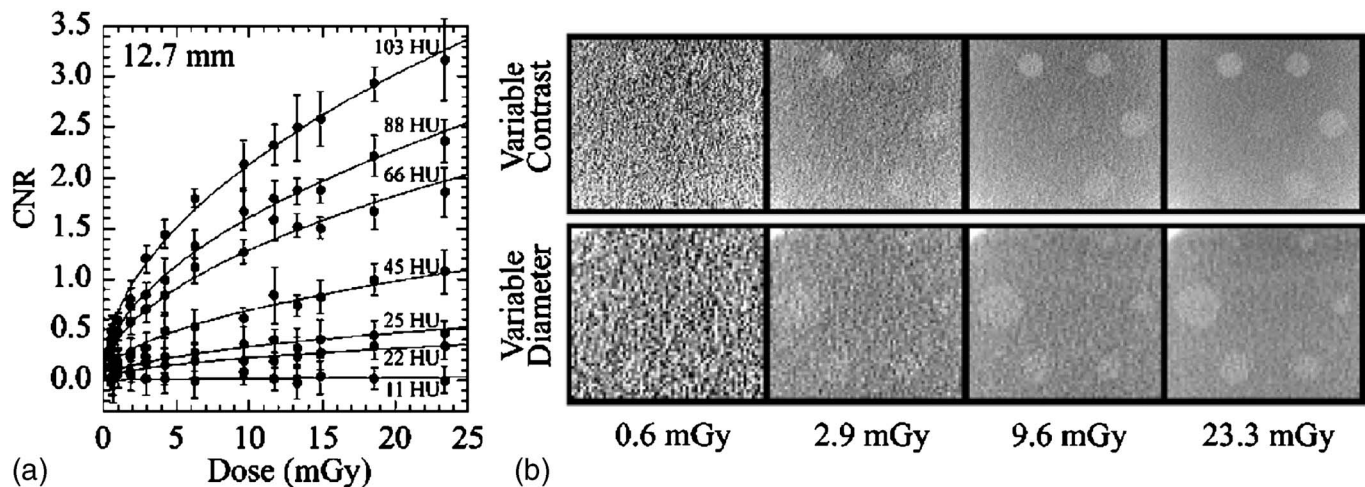


FIG. 7. *Effect of CBCT dose on soft-tissue visualization:* (a) CNR as a function of imaging dose in spheres of variable contrast (11–103 HU; 12.7 mm diameter) contained within the anthropomorphic skull. (b) Axial images from 3D volume reconstructions illustrating visualization performance in contrast-detail spheres of variable contrast (11–103 HU; 12.7 mm diameter; top row) and variable diameter (1.6–12.7 mm; 84 HU; bottom row) across a range of imaging dose (0.6–23.3 mGy). The seven curves in (a) correspond to the seven variable-contrast spheres in (b) (top row), with the 25 HU sphere in the center and the remaining spheres (11 to 103 HU) arranged counter-clockwise from left. The variable-diameter spheres in (b) (bottom row) range 12.7 to 3.2 mm, arranged counterclockwise from left, with an additional three 1.6 mm spheres placed near center.

structures are still clearly distinguished (e.g., the sella turcica that delineates the pituitary gland). Also, the phantom has sinuses filled with water-equivalent material, rather than air filled, and therefore, visualization of sinus air cells would be somewhat better in more realistic, air-filled sinuses. The images at dose levels 2.9–23.3 mGy indicate that the majority of bony structures in both the sinuses and skull base are clearly visible at ~ 3 mGy and above.

2. Effect of number of projections

Figure 9 demonstrates the effect of the number of projections ($N_{\text{proj}} = 100, 200$, or 500) acquired during CBCT acquisition on imaging performance. In Fig. 9(a), CNR is plotted as a function of N_{proj} at three dose levels (~ 1.5 , ~ 3.6 , and ~ 11.7 mGy). No effect of view aliasing-related noise on CNR is observed, as demonstrated in images of the variable-contrast (fixed-diameter) spheres (nominal 0.8 mm voxel size) in Fig. 9(b), and of the temporal bone region (0.2 mm

voxel size) in Fig. 9(c). In neither case is there evidence of significant view aliasing (radial streak) artifacts. A reproducible increase in noise for $N_{\text{proj}} = 100$ at ~ 11.71 mGy is observed ($p = 0.03$), however, the correlated noise observed in Figs. 9(b) and 9(c) does not appear to be a view aliasing artifact; rather, it appears to be associated with ring artifacts. The source of this artifact is under investigation, and may be associated with a high dose per projection and imperfect flood-field correction in DGI mode.

3. Effect of reconstruction filter

Figure 10 illustrates the quantitative and qualitative effect of the reconstruction filter on CBCT image quality. Figure 10(a) shows the CNR for the 103 HU (12.7 diameter) sphere as a function of CBCT dose for four reconstruction filters ($H = 0.11$ – 0.66). Reducing the cut-off frequency H has the effect of increasing CNR due to smoothing of image noise.

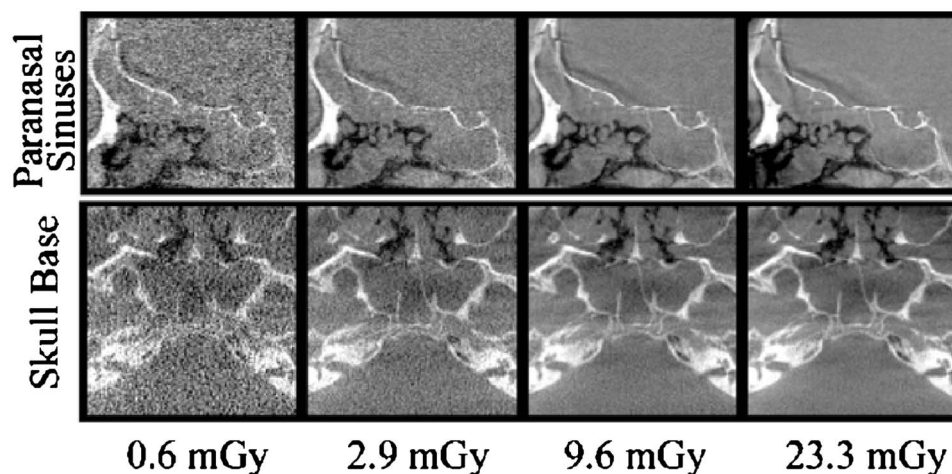


FIG. 8. *Effect of CBCT dose on bony anatomy visualization:* Sagittal images of the paranasal sinuses (including the frontal sinus, ethmoid air cells, cribriform plate, pituitary gland, sphenoid sinus, and clivus) and axial images of the skull base (including the sphenoid sinus and clivus) from 3D volume reconstructions across a range of imaging dose (0.6–23.3 mGy).

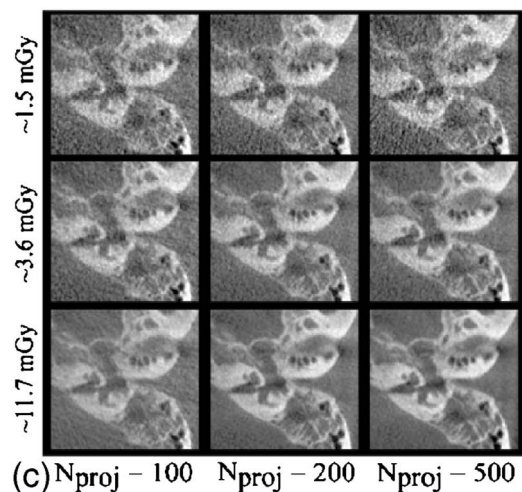
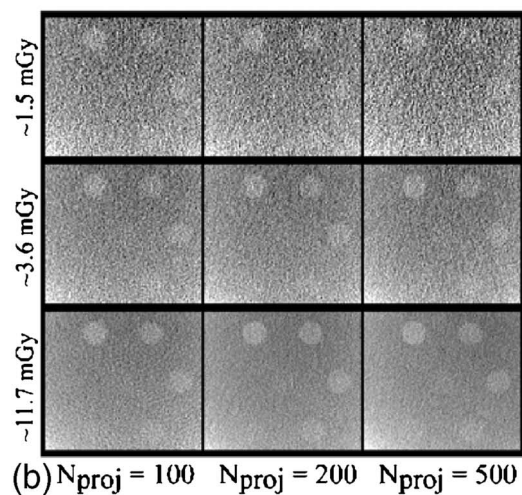
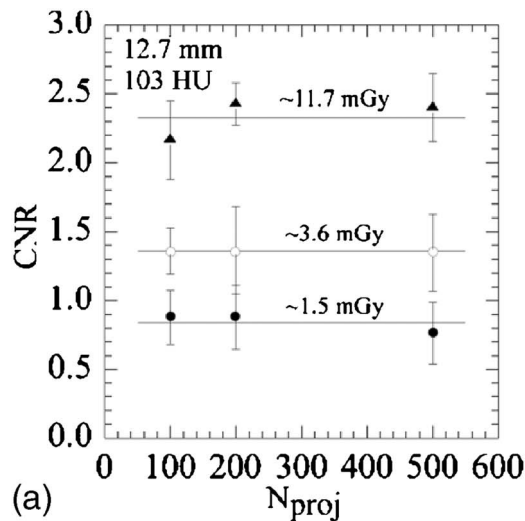


FIG. 9. Effect of number of projections on CBCT image quality: (a) CNR as a function of number of projections (N_{proj}) for three imaging doses (~ 1.5 , ~ 3.6 , ~ 11.6 mGy). (b) Axial images of soft-tissue structures (variable-contrast, fixed-diameter spheres) reconstructed with the nominal voxel size (0.8 mm). (c) Axial images of the temporal bone (including the mastoid air cells, external auditory canal, and cochlea) using a reconstruction voxel size of 0.2 mm, chosen to provide improved visualization of fine detail in the temporal bone and to better illustrate the degree of view aliasing artifacts.

Image noise was found to increase linearly with H at each imaging dose with no significant change in contrast, resulting in CNR variation as the inverse of H .

Axial images of soft-tissue structures (variable-contrast, fixed-diameter spheres) and bony anatomy (skull base) acquired at an imaging dose of 2.9 mGy are shown in Fig. 10(b). At 2.9 mGy, the CNR varied from 1.2 to 14.3 over the range $H=0.11$ – 0.66 . Visibility of soft-tissue structures is highest for $H=0.11$ (“smooth”), but the images display significant blurring of the bony anatomy as seen in the poor delineation of the clivus and sphenoid sinus wall. At the other extreme, the images using $H=0.66$ (“sharp”) provide the highest spatial resolution; however, detectability of the lower contrast spheres, most noticeably the 45 HU sphere, is more challenging.

As expected, the choice of parameter H is subject to an inherent tradeoff between image sharpness and noise, and clearly there exists the opportunity in some cases to select the reconstruction filter to best accommodate the imaging task. Image-guided surgery experiments at our institution have found the choice of $H=0.33$ – 0.66 sufficient for guidance of spinal¹³ and head and neck¹⁶ procedures. Except for the images noted in Fig. 10, all soft-tissue and bony anatomy images (Figs. 7–11) used a reconstruction filter with $H=0.66$. It is noted that the reconstruction filter has a nonisotropic effect on image quality, with the tradeoff between image sharpness and noise observable in the axial (x - y) plane, but only partly evident in the sagittal (y - z) and coronal (x - z) planes.³¹

4. Effect of voxel size

The effect of voxel size (four settings of axial slice averaging) on CBCT image quality is presented in Fig. 11. CNR for a 103 HU, 12.7 mm sphere is shown in Fig. 11(a) as a function of dose for four axial slice thicknesses ($\Delta z_{slice}=0.8$ – 3.2 mm). Increasing the slice thickness Δz_{slice} increases the CNR due to averaging of noise across adjacent slices. Image noise varied as the inverse of $\sqrt{\Delta z_{slice}}$, without effect on absolute contrast, resulting in CNR variation as $\sqrt{\Delta z_{slice}}$, which agrees with theoretical expectation.³⁰

Axial images of variable-contrast (fixed-diameter) spheres and skull base bony anatomy at an imaging dose of 2.9 mGy are shown in Fig. 11(b). At 2.9 mGy, the CNR varied from 1.2 to 2.2 over the range $\Delta z_{slice}=0.8$ – 3.2 mm. The images with $\Delta z_{slice}=0.8$ mm are the nominal setting with no slice averaging (e.g., Figs. 7–10). While soft-tissue visualization improves with increasing Δz_{slice} , slice averaging also introduces significant image blur, as evident in the reduced visibility of bony trabeculae in the clivus at $\Delta z_{slice}=3.2$ mm. Similarly, the potential for partial volume artifacts is increased for greater values of Δz_{slice} .

IV. DISCUSSION AND CONCLUSIONS

Table I summarizes the dosimetry associated with CBCT scan techniques sufficient for visualization of (i) high-contrast bony anatomy only and (ii) high-contrast bone and low-contrast soft-tissue. Absolute and effective dose values

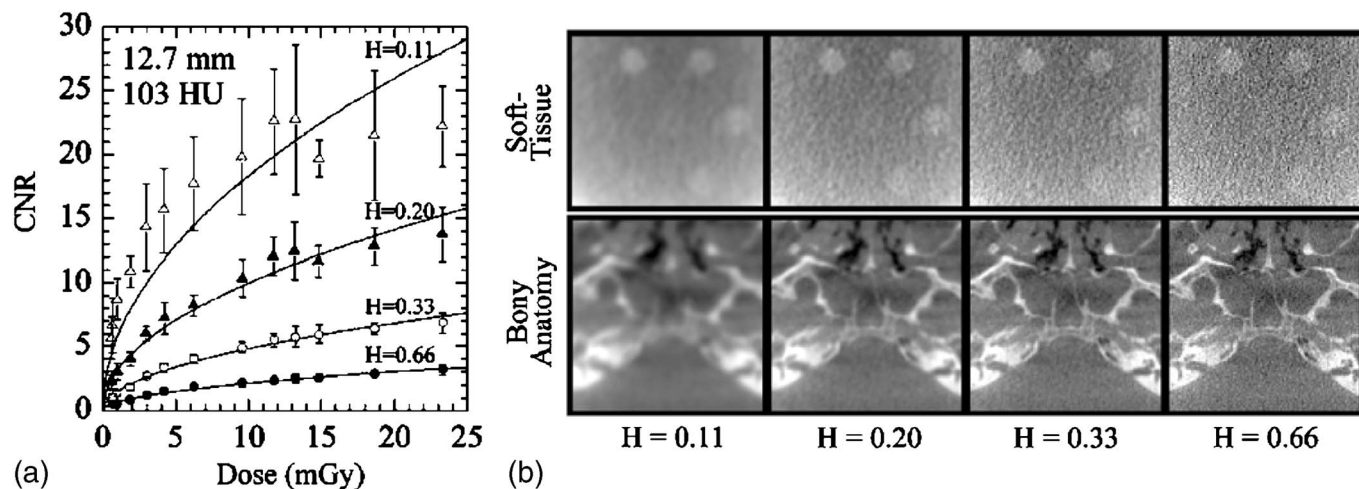


FIG. 10. Effect of reconstruction filter on CBCT image quality: (a) CNR (in a sphere of 103 HU contrast and 12.7 mm diameter) as a function of CBCT dose for four reconstruction filters (relative cutoff frequencies, $H=0.11$ – 0.66). (b) Axial images of soft-tissue structures (variable-contrast, fixed-diameter spheres) and bony anatomy (skull base) at 2.9 mGy illustrating visualization performance as a function of H .

are shown for both the patient (various positions within the head) and staff (various locations within the room).

A. Intraoperative dose to patient

A frequently reported effective dose (E) for a diagnostic head CT scan is 2 mSv, with a range of values (~ 1 – 5 mSv)^{25,32–34} resulting from variability in clinical protocols (e.g., kVp, mAs, collimation, number of slices, pitch), CT technology (e.g., multidetector designs, automatic exposure control), and patient characteristics. In this paper, the effect of CBCT dose on image quality was assessed over the range 0.6–23.3 mGy, which corresponds to effective doses of 0.02–0.80 mSv, or 1–40 % of a nominal 2 mSv diagnostic head CT scan. The assessment of CBCT image quality concluded that sufficient guidance with respect to the visualization of soft-tissue structures and bony anatomy was pro-

vided for doses ~ 10 mGy (0.35 mSv, or 18% of a nominal head CT) and ~ 3 mGy (0.10 mSv, or 5%), respectively. These results demonstrate that the radiation doses for CBCT acquisition are sufficiently low to allow for repeat intraoperative imaging during a head and neck procedure with less radiation risk than a nominal 2 mSv diagnostic CT of the head. The frequency of intraoperative CBCT acquisition and the accumulated radiation dose is discussed below. For a “tube-under” CBCT acquisition there is significantly less dose at the anterior (i.e., eye lenses) than the posterior, suggesting strategies for dose reduction in both interventional CBCT and diagnostic CT head scans (below). In this sense, the dose comparison of CBCT (acquired in a “tube-under” orbit) to a typical diagnostic CT head scan (acquired in a 360° orbit) can be seen as a conservative estimate of effective dose, since the former entails a lower dose to the eyes.

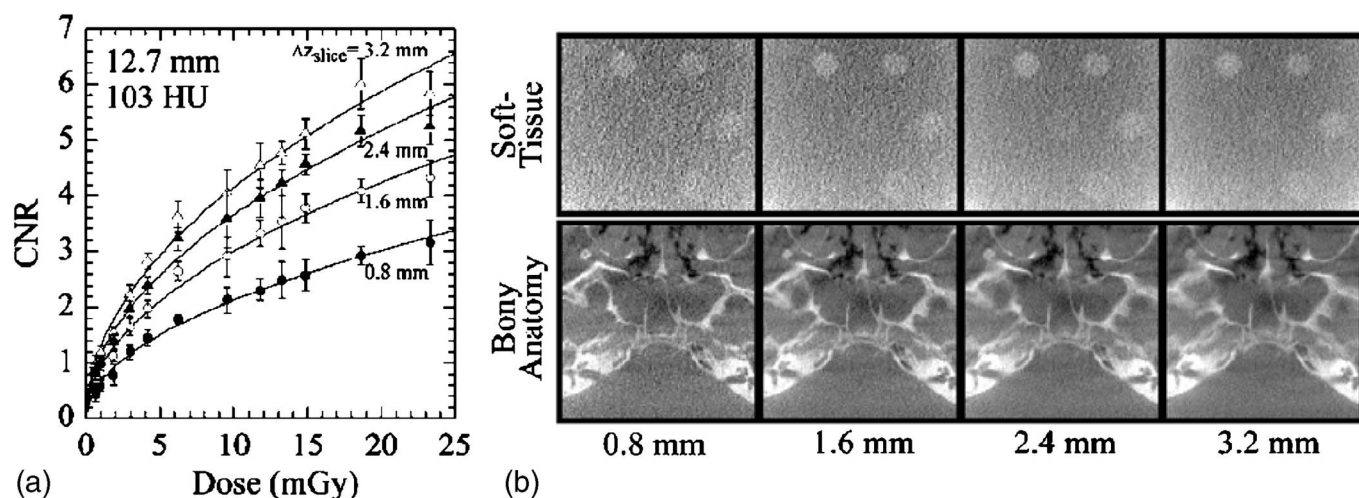


FIG. 11. Effect of slice averaging on CBCT image quality: (a) CNR (in a sphere of 103 HU contrast and 12.7 mm diameter) as a function of CBCT dose for four axial slice thicknesses ($\Delta z_{\text{slice}}=0.8$ – 3.2 mm). (b) Axial images of soft-tissue structures (variable-contrast, fixed-diameter spheres) and bony anatomy (skull base) at 2.9 mGy illustrating visualization performance as a function of Δz_{slice} .

TABLE I. Summary of dosimetry for CBCT techniques sufficient for visualization of (i) high-contrast bony anatomy only and (ii) high-contrast bone and low-contrast soft-tissue. Absolute and effective dose are shown for positions in the head phantom (A-anterior, B-posterior, C-isocenter, D-lateral, as illustrated in Fig. 1). In-air exposure and effective dose (unshielded and shielded) are shown for various locations within the room (T2 at 35 cm superior of isocenter, T4 at 40 m lateral of isocenter, and locations at 1 and 2 m from isocenter, as shown in Fig. 6). Results correspond to “tube-under” half-rotation orbit at 100 kVp.

CBCT scan protocol	Patient dose (head phatom)					In-room exposure (in-air)							
	Absolute dose (mGy)				Effective dose (mSv)	X(mR)				$E_{\text{unshielded}}$ (mSv) [E_{shielded} (mSv)]			
	A	B	C	D		T2	T4	1 m	2 m	T2	T4	1 m	2 m
Bony visualization (50 mAs)	1.1	5.0	3.0	2.8	0.10	8.6	4.7	0.9	0.1	0.078 [0.015]	0.042 [0.008]	0.008 [0.0015]	0.002 [0.0002]
Soft-tissue visualization (170mAs)	3.7	17	10	9.5	0.35	29	16	2.9	0.4	0.26 [0.05]	0.14 [0.03]	0.03 [0.005]	0.004 [0.0007]

B. Dose reduction strategies for CT acquisition

The “tube-under” orbit for CBCT acquisition demonstrates two significant advantages over a “tube-over” orbit: A significant dose sparing to the eyes is achieved (a factor of >5), and in the presence of a patient support it gives higher image quality per unit patient dose. The clear benefits of a “tube-under” half-rotation orbit also suggest opportunities for dose reduction in diagnostic CT systems. For example, existing current modulation and automatic exposure control (AEC) methods³⁵ can provide dose reduction by compensating for variations in patient diameter and attenuation (e.g., LAT versus AP views of the pelvis), but the ability to modulate x-ray tube current to compensate for variations in organ radiosensitivity could provide further dose sparing (e.g., for the head, reduced tube current in AP views). Further, modulation in which current is restricted to projections acquired over $\sim 180^\circ$ – 270° is equivalent to various “half-scan” and “limited orbit” techniques,^{36,37} which have been proposed primarily for purposes of increased scan speed; however, implementation such that the current is disabled outside the limited orbit (e.g., disabled in AP views) could be employed to provide dose sparing to the eyes during head CT, as well as other radiosensitive structures (e.g., the breasts during a thoracic CT). The image quality associated with such orbits is certainly important; however, image quality and scan speed should be considered in combination with the potential for reduced effective dose. More sophisticated modeling of effective dose (e.g., Monte Carlo calculation of organ-specific conversion factors for the eyes) would help to further quantify the dosimetric advantages of half-scan orbits and facilitate further dose reduction strategies.

C. CT-compatible patient supports

To examine the effect of patient supports on CBCT dose, three representative tables were characterized as illustrative examples. In general, the dose reduction associated with a given head and neck support is dependent on its shape, width, thickness, and material composition, and can there-

fore vary substantially. For clinical implementation, a CT-compatible stereotactic frame (e.g., carbon fiber composition with no metal structures) affixed to the skull would provide greater access to the patient for a range of procedures (e.g., combined otolaryngology and neurosurgery approaches). Such frames are already in clinical use, some CT compatible, and an increased role of such in CBCT-guided procedures is evident. The measurements reported above for dose to the head (supported in air), combined with the dose reduction factors associated with various patient supports, provide a portable characterization of intraoperative CBCT patient dose, with the nominal head-in-air measurements close to the ideal case of a minimally obtrusive, CT-compatible stereotactic head frame.

D. Intraoperative in-room exposure to surgical staff

As with all radiology procedures, only personnel whose presence is clinically necessary should be in the surgical suite during operation of the x-ray tube. For cases in which it is not possible for surgical staff to leave the room, it is necessary to ensure the in-room exposure is as low as reasonably achievable during CBCT acquisition. The International Commission on Radiological Protection (ICRP) recommends annual exposure limits of 20 mSv/yr for occupational staff and 1 mSv/yr for members of the public.³⁸ In-room unshielded effective dose ($E_{\text{unshielded}}$) measured in-air for a 10 mGy CBCT scan ranged from 0.26 mSv at 35 cm from the isocenter, to <0.005 mSv at 2 m, with the potential for dose reduction with increased distance evident. Estimates of the shielded effective dose (E_{shielded}) using a 0.5 mm Pb-equivalent apron and thyroid shield are ~ 0.06 mSv at 35 cm, and $< \sim 0.001$ mSv at 2 m, based on calculations from in-air exposure measurements. At minimum, staff positions should be sufficiently outside the imaging FOV not only to avoid direct contact with primary radiation, but also to avoid introducing artifacts in CBCT reconstructions and to prevent collision with the C-arm gantry during orbital motion. The need for personnel radiation protection and modu-

lar shield walls in the surgical suite to limit exposure levels are clear, in accordance with regulatory requirements.

Unshielded CBCT exposure rates around the operating table (e.g., $E_{\text{unshielded}} = 0.26$ mSv at 35 cm distance, measured over a 60 s scan) are comparable to exposures in orthopaedic surgery during C-arm fluoroscopy, with one study reporting a range of 0.06–0.29 mSv/min measured at distances 30–70 mm for an AP exposure rate of 40 mSv/min (in-air at isocenter),³⁹ and a second study reporting rates of 0.05 mSv/min at 60 cm and 0.01 mSv/min at 1.25 m due to scattered radiation with a typical total acquisition time of 5 min.⁴⁰ Prolonged exposure during interventional radiology procedures can result in greater risk to staff than other radiology examinations,⁴¹ with unshielded exposure rates in interventional cardiology of 0.017–0.23 mSv/min for fluoroscopy and 0.17–0.78 mSv/min for cine acquisition reported.⁴² The use of radiation protection methods (e.g., personnel shielding, protective screens, and training for staff in radiation protection) have demonstrated reductions in radiation doses to interventional cardiology staff to 1.2 mSv/yr.⁴¹

E. Image quality

Qualitative assessment of image quality suggests that CBCT imaging performance sufficient for interventional guidance with respect to soft-tissue and bony anatomy was achieved at doses $< \sim 10$ mGy and $< \sim 3$ mGy, respectively. The effects of CBCT acquisition and reconstruction parameters on 3D image quality agreed with theoretical expectations: CNR increased as the square root of dose, decreased as the inverse of the reconstruction filter relative cut-off frequency, increased as the square root of voxel size, and was not affected by the number of projections (over the range 100–500). The demonstrated tradeoffs in image noise and sharpness indicate that there exists sufficient flexibility to tailor acquisition (e.g., kVp, mA, N_{proj} , scan time) and reconstruction (e.g., reconstruction filter, voxel size) parameters to the specific imaging task and clinical constraints (e.g., time and dose). This motivates the use of an adaptable post-processing framework for intraoperative imaging to allow for improved visualization of soft-tissue (e.g., via smooth filters and increased voxel size) and bony structures (e.g., via sharp filters and reduced voxel size), built on a high-performance computing and visualization infrastructure.

F. Models for intraoperative use

Based on preclinical studies and looking forward to clinical implementation, we estimate at least two scans per procedure (e.g., one preoperative and one postoperative), with additional intraoperative scans acquired as needed to provide intraoperative image updates. The integration of the C-arm CBCT imaging system with an in-room tracking and navigation system is expected to reduce the frequency of repeat intraoperative image acquisition, depending on the degree of morphological deformation to the anatomy over the course of the procedure. The potential also exists for dose reduction during intraoperative imaging by reducing the FOV confor-

mal to the clinical region of interest,⁴³ with the 3D information necessary to prescribe a FOV provided by the combination of previous preoperative/intraoperative scans and the in-room navigation system. The incorporation of an automatic aperture (e.g., automatic brightness control) in the C-arm system could offer further dose reduction (similar to current modulation) by adapting the x-ray tube current (and/or kVp) to provide a specified detector signal in all projection views.

The CBCT image quality assessment suggests the use of a ~ 10 mGy (0.35 mSv) CBCT scan for visualization of both soft-tissue and bony anatomy for preoperative setup/planning and postoperative verification. Consideration of the imaging task should influence the selection of dose during intraoperative imaging, which would allow some scans requiring only guidance with respect to bony anatomy to be acquired with patient doses as low as $< \sim 3$ mGy (0.10 mSv). Thus, ~ 5 – 6 “soft-tissue” scans or ~ 20 “bony visualization” scans (See Table I) could be performed with total dose comparable to that of a 2 mSv diagnostic head CT. A possible scenario, for example, could involve four “soft-tissue” scans (~ 0.35 mSv each; one preoperative, two intraoperative, and one postoperative) and six “bony visualization” scans (~ 0.10 mSv each) with total effective dose equal to that of a nominal 2 mSv diagnostic head CT.

ACKNOWLEDGMENTS

This work was conducted in research collaboration with Siemens Medical Systems, Special Products Group (Erlangen, Germany), with the scientific and engineering support of Dr. R. Graumann, Dr. K. Hermann, Dr. D. Ritter, and Dr. M. Mitschke. The authors extend thanks to Dr. Christopher Paige (Ontario Cancer Institute) for his support of this research. Thanks to Dr. R. Moukarbel (University Health Network) for discussions on clinical aspects of image-guided head and neck surgery. Dr. Mohammad Islam, Ralph Strohschein, and Judy Reid (University Health Network) are gratefully acknowledged for assistance with dosimetry equipment. Thanks also to S. Ansell and G. Wilson for expertise and assistance with software components of the imaging system. This work was supported in part by the National Institute of Health (R01-EB002470-04) and the University of Toronto New Staff Award (No. 72022001).

^{a)}Corresponding author; electronic address: jsiewerd@uhnres.utoronto.ca
¹R. Metson, R. Cosenza, R. E. Gliklich, and W. W. Montgomery, “The role of image-guidance systems for head and neck surgery,” *Arch. Otolaryngol. Head Neck Surg.* **125**(10), 1100–1104 (1999).

²R. Sindwani and R. Metson, “Image-guided frontal sinus surgery,” *Otolaryngol. Clin. North Am.* **38**(3), 461–471 (2005).

³T. T. Kingdom and R. R. Orlandi, “Image-guided surgery of the sinuses: Current technology and applications,” *Otolaryngol. Clin. North Am.* **37**(2), 381–400 (2004).

⁴W. Freysinger, A. R. Gunkel, and W. F. Thumfart, “Image-guided endoscopic ENT surgery,” *Eur. Arch. Otorhinolaryngol.* **254**(7), 343–346 (1997).

⁵M. K. Gibson and A. A. Forastiere, “Multidisciplinary approaches in the management of advanced head and neck tumors: State of the art,” *Curr. Opin. Oncol.* **16**(3), 220–224 (2004).

⁶R. J. Schlosser and W. E. Bolger, “Image-guided procedures of the skull base,” *Otolaryngol. Clin. North Am.* **38**(3), 483–490 (2005).

⁷M. J. Citardi and P. S. Batra, “Image-guided sinus surgery: Current con-

- cepts and technology," *Otolaryngol. Clin. North Am.* **38**(3), 439–452, (2005).
- ⁸M. Cartellieri and F. Vorbeck, "Endoscopic sinus surgery using intraoperative computed tomography imaging for updating a three-dimensional navigation system," *Laryngoscope* **110**(2 Pt 1), 292–296 (2000).
- ⁹M. P. Fried, G. Topulos, L. Hsu, H. Jalahej, H. Gopal, A. Lauretano, P. R. Morrison, and F. A. Jolesz, "Endoscopic sinus surgery with magnetic resonance imaging guidance: Initial patient experience," *Arch. Otolaryngol. Head Neck Surg.* **119**(4), 374–380 (1998).
- ¹⁰D. A. Jaffray and J. H. Siewerdsen, "Cone-beam computed tomography with a flat-panel imager: Initial performance characterization," *Med. Phys.* **27**(6), 1311–1323 (2000).
- ¹¹J. H. Siewerdsen, D. A. Jaffray, G. K. Edmundson, W. P. Sanders, J. W. Wong, and A. Martinez, "Flat-panel cone-beam CT: A novel imaging technology for image-guided procedures," *Proc. SPIE* **4319**, 435–444 (2001).
- ¹²D. A. Jaffray, J. H. Siewerdsen, G. K. Edmundson, J. W. Wong, and A. Martinez, "Flat-panel cone-beam CT on a mobile isocentric C-arm for image-guided brachytherapy," *Proc. SPIE* **4682**, 209–217 (2002).
- ¹³J. H. Siewerdsen, D. J. Moseley, S. Burch, S. K. Bisland, A. Bogaards, B. C. Wilson, and D. A. Jaffray, "Volume CT with a flat-panel detector on a mobile, isocentric C-arm: Pre-clinical investigation in guidance of minimally invasive surgery," *Med. Phys.* **32**(1), 241–254 (2005).
- ¹⁴A. Khoury, C. M. Whyne, M. J. Daly, D. J. Moseley, G. Bootsma, T. Skrinskas, J. H. Siewerdsen, and D. A. Jaffray, "Intraoperative cone-beam CT for correction of periaxial malrotation of the femoral shaft: A surface-matching approach," *ORS 52nd Annual Meeting*, Chicago, IL (Orthopaedic Research Society, Rosemont, IL, 2006).
- ¹⁵A. Khoury, C. M. Whyne, M. J. Daly, D. J. Moseley, G. Bootsma, T. Skrinskas, J. H. Siewerdsen, and D. A. Jaffray, "Intraoperative cone-beam CT for correction of periaxial malrotation of the femoral shaft: A surface-matching approach," *Med. Phys.* (submitted).
- ¹⁶J. H. Siewerdsen, Y. Chan, M. A. Rafferty, D. J. Moseley, D. A. Jaffray, and J. C. Irish, "Cone-beam CT with a flat-panel detector on a mobile C-arm: Preclinical investigation in image-guided surgery of the head and neck," *Proc. SPIE* **5744**, 789–797 (2005).
- ¹⁷Y. Chan, J. H. Siewerdsen, M. A. Rafferty, D. J. Moseley, D. A. Jaffray, and J. C. Irish, "Cone-beam, CT on a mobile C-arm: A novel intraoperative imaging technology for guidance of head and neck surgery," *J. Otolaryngol.* (in press).
- ¹⁸M. A. Rafferty, J. H. Siewerdsen, Y. Chan, M. J. Daly, D. J. Moseley, D. A. Jaffray, and J. C. Irish, "Intraoperative cone-beam CT for guidance of temporal bone surgery," *Otolaryngol.-Head Neck Surg.* **134**(5), 801–808 (2006).
- ¹⁹M. A. Rafferty, J. H. Siewerdsen, Y. Chan, D. J. Moseley, M. J. Daly, D. A. Jaffray, and J. C. Irish, "Investigation of C-arm cone-beam CT-guided surgery of the frontal recess," *Laryngoscope* **115**(12), 2138–2143 (2005).
- ²⁰P. G. Roos, R. E. Colbeth, I. Molloy, P. Munro, J. M. Pavkovich, E. Seppi, E. G. Shapiro, C. A. Tognina, G. Virshup, M. Yu, G. Zentai, W. Kaissl, E. Matsinos, J. Richters, and H. Riem, "Multiple gain ranging readout method to extend the dynamic range of amorphous silicon flat panel imagers," *Proc. SPIE* **5368**, 139–149 (2004).
- ²¹L. A. Feldkamp, L. C. Davis, and J. W. Kress, "Practical cone-beam algorithm," *J. Opt. Soc. Am. A* **1**, 612–619 (1984).
- ²²M. Mitschke and N. Navab, "Optimal configuration for dynamic calibration of projection geometry of x-ray C-Arm systems," *IEEE Workshop on Mathematical Methods in Biomedical Image Analysis (MMBIA)* (IEEE, Hilton Head, SC, 2000).
- ²³J. H. Hubbell, "Photon Mass Attenuation and Energy-Absorption Coefficients from 1 keV to 20 MeV," *Int. J. Appl. Radiat. Isot.* **33**, 1269–1290 (1982).
- ²⁴C. M. Ma, C. W. Coffey, L. A. DeWerd, C. Liu, R. Nath, S. M. Seltzer, and J. P. Seuntjens, "AAPM protocol for 40–300 kV x-ray beam dosimetry in radiotherapy and radiobiology," *Med. Phys.* **28**(6), 868–893 (2001).
- ²⁵European Commission, "Quality criteria for computed tomography," EUR 16262 (European Commission, Luxembourg, 1999) <http://www.dr.dk/guidelines/ct/quality/mainindex.htm>
- ²⁶F. M. Khan, *The Physics of Radiation Therapy* (Williams & Wilkins, Baltimore, MD, 1984).
- ²⁷E. W. Webster, "EDE for exposure with protective aprons," *Health Phys.* **56**(4), 568–569 (1989).
- ²⁸J. T. Bushberg, J. A. Seibert, E. M. Leidholdt, Jr., and J. M. Boone, *The Essential Physics of Medical Imaging*, 2nd Ed. (Williams & Wilkins, Baltimore, MD, 1994).
- ²⁹C. B. Chiarot, J. H. Siewerdsen, T. Haycocks, D. J. Moseley, and D. A. Jaffray, "An innovative phantom for quantitative and qualitative investigation of advanced x-ray imaging technologies," *Phys. Med. Biol.* **50**(21), N287–N297 (2005).
- ³⁰H. H. Barrett, S. K. Gordon, and R. S. Hershel, "Statistical limitations in transaxial tomography," *Comput. Biol. Med.* **6**(4), 307–323 (1976).
- ³¹J. H. Siewerdsen, I. A. Cunningham, and D. A. Jaffray, "A framework for noise-power spectrum analysis of multidimensional images," *Med. Phys.* **29**(11), 2655–2671 (2002).
- ³²U. S. Food and Drug Administration (FDA) and Conference of Radiation Control Program Directors Inc. (CRCPD). "Nationwide Evaluation of X-Ray Trends (NEXT) 2000 Computed Tomography Trifold," <http://www.crcpd.org/Pubs/NextTrifolds/NEXT2000CT.T.pdf> (2006).
- ³³F. A. Mettler, Jr., P. W. Wiest, J. A. Locken, and C. A. Kelsey, "CT scanning: Patterns of use and dose," *J. Radiol. Prot.* **20**(4), 353–359 (2000).
- ³⁴W. Huda, C. C. Chamberlain, A. E. Rosenbaum, and W. Garrisi, "Radiation doses to infants and adults undergoing head CT examinations," *Med. Phys.* **28**(3), 393–399 (2001).
- ³⁵W. A. Kalender, H. Wolf, and C. Suess, "Dose reduction in CT by anatomically adapted tube current modulation. II. Phantom measurements," *Med. Phys.* **26**(11), 2248–2253 (1999).
- ³⁶S. W. Lee and G. Wang, "Grangeat-type helical half-scan computerized tomography algorithm for reconstruction of a short object," *Med. Phys.* **31**(1), 4–16 (2004).
- ³⁷L. Yu and X. Pan, "Half-scan fan-beam computed tomography with improved noise and resolution properties," *Med. Phys.* **30**(10), 2629–2637 (2003).
- ³⁸International Commission on Radiological Protection (ICRP), "1990 Recommendations of the International Commission on Radiological Protection. ICRP Publication No. 60," *Annals of the ICRP* **21** (1991).
- ³⁹C. T. Mehlman and T. G. DiPasquale, "Radiation exposure to the orthopaedic surgical team during fluoroscopy: How far away is far enough?," *J. Orthop. Trauma* **11**(6), 392–398 (1997).
- ⁴⁰G. Singer, "Occupational radiation exposure to the surgeon," *J. Am. Acad. Orthop. Surg.* **13**(1), 69–76 (2005).
- ⁴¹E. Vano, L. Gonzalez, J. M. Fernandez, F. Alfonso, and C. Macaya, "Occupational radiation doses in interventional cardiology: A 15-year follow-up," *Br. J. Radiol.* **79**(941), 383–388 (2006).
- ⁴²E. Vano, L. Gonzalez, J. M. Fernandez, C. Prieto, and E. Guibelalde, "Influence of Patient Thickness and Operation Modes on Occupational and Patient Radiation Doses in Interventional Cardiology," *Radiat. Prot. Dosim.* **118** (3), 325–330 (2006).
- ⁴³Y. Zou, X. Pan, and E. Y. Sidky, "Image reconstruction in-regions-of-interest from truncated projections in a reduced fan-beam scan," *Phys. Med. Biol.* **50**(1), 13–27 (2005).



**We drive the development
of solutions for safer
radiation therapy**



**DELIVERY DOSAGE
ENSURED**

**INDEPENDENT VERIFICATION
DURING TREATMENT**

**OPTIMIZED CLINICAL
WORKFLOW**

A complete solution for all your patient QA needs

The Delta4 Family of products delivers Quality Assurance from prescription to final fraction.

Not only can you expect to increase your workflow efficiency but, most importantly, you can also carry out your work with full confidence that the treatment dose delivered to your patient is safe.

The Delta4 Family covers all modern treatment technologies, including VMAT, IMRT, SRS/SBRT, 4D-RT, MRgRT, bore-based linacs, Radixact and TomoTherapy.



*Innovative and Efficient QA
Delta4family.com*